Oxide Ion Conductor | Hot Paper

DOI: 10.1002/anie.201402244

A Metallic Room-Temperature Oxide Ion Conductor**

Martin Heise, Bertold Rasche, Anna Isaeva, Alexey I. Baranov, Michael Ruck, Konrad Schäfer, Rainer Pöttgen, Jens-Peter Eufinger, and Jürgen Janek*

Abstract: *Nanoparticles of Bi_3Ir, obtained from a microwave-assisted polyol process, activate molecular oxygen from air at room temperature and reversibly intercalate it as oxide ions. The closely related structures of Bi_3Ir and Bi_3IrO_x ($x \leq 2$) were investigated by X-ray diffraction, electron microscopy, and quantum-chemical modeling. In the topochemically formed metallic suboxide, the intermetallic building units are fully preserved. Time- and temperature-dependent monitoring of the oxygen uptake in an oxygen-filled chamber shows that the activation energy for oxide diffusion (84 meV) is one order of magnitude smaller than that in any known material. Bi_3IrO_x is the first metallic oxide ion conductor and also the first that operates at room temperature.*

Intercalation chemistry is typically associated with layered systems such as graphite, transition-metal dichalcogenides, double hydroxides, and clays (phyllosilicates).[1–4] Electrochemical lithium intercalation was and is still widely investigated for battery applications. From a phenomenological view the same holds for oxygen with a focus on nonstoichiometric oxides in, for example, solid oxide fuel-cell electrodes and sensors. Yet, nobody has ever observed a fully reversible uptake of oxygen into an intermetallic compound.

Here we report on nanoparticles of Bi_3Ir, a hitherto uncharacterized intermetallic compound, that instantly take up oxygen from air at room temperature. This is, however, not the simple transformation to common oxides, but a fast topochemical redox intercalation of molecular oxygen from air. The process can easily be monitored by powder X-ray diffraction (PXRD; Figure 1): within few hours the diffraction pattern of the intermetallic compound changes to that of a phase with the composition Bi_3IrO_x ($x \leq 2$). Thereby, the intensities of the diffraction peaks remain mostly unchanged while their positions move towards lower angles. In fact, the unit cell increases in size while oxygen is intercalated in between the $[Bi_3Ir]$ rods that constitute the structures of both the innocent host and the loaded phase (Figure 2). The redox intercalation is fully reversible. Treatment of Bi_3IrO_x with hydrazine at room temperature or with hydrogen gas at 150 °C removes the oxygen and restores the initial structure of the intermetallic compound.

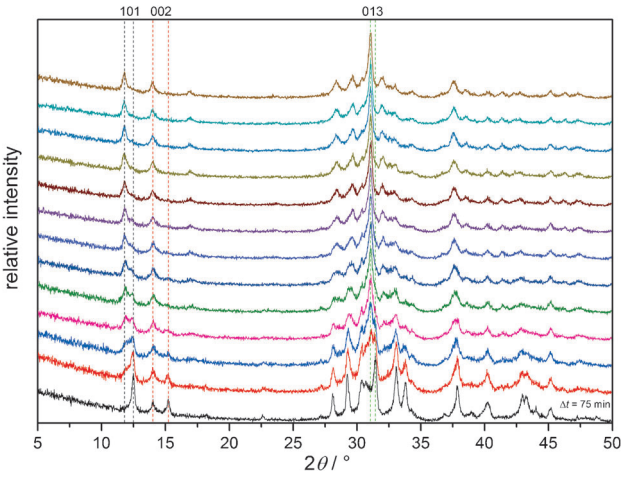

Figure 1. The time-dependent oxidation of Bi_3Ir to Bi_3IrO_x at room temperature was monitored by X-ray powder diffraction. The process is associated with an expansion of the lattice, which can be followed, e.g., by the shifts of the reflections 002 and 101 to lower angles. The time interval between consecutive measurements is 75 min. Further diffractograms for as-synthesized Bi_3Ir as well as for Bi_3IrO_x after 15 h and after one year exposure to air see Figures S1–S3 in the Supporting Information.

One reason why the reversible absorption of oxygen by Bi_3Ir has not been observed earlier is that this intermetallic

[*] M. Heise, B. Rasche, Dr. A. Isaeva, Dr. A. I. Baranov, Prof. Dr. M. Ruck
Fachrichtung Chemie und Lebensmittelchemie
Technische Universität Dresden
01062 Dresden (Germany)
E-mail: michael.ruck@tu-dresden.de
Prof. Dr. M. Ruck
Max Planck Institut für Chemische Physik fester Stoffe
Nöthnitzer Strasse 40, 01187 Dresden (Germany)
K. Schäfer, Prof. Dr. R. Pöttgen
Institut für Anorganische und Analytische Chemie
Universität Münster
Corrensstrasse 30, 48149 Münster (Germany)
J.-P. Eufinger, Prof. Dr. J. Janek
Institut für Physikalische Chemie
Justus-Liebig-Universität Gießen
Heinrich-Buff-Ring 58, 35392 Gießen (Germany)

[**] We gratefully acknowledge Dr. I. Kunert (TU Dresden) for DSC measurements. We are indebted to ZIH TU Dresden for computational facilities. We gratefully acknowledge Prof. U. Kaiser, Prof. C. T. Koch, and Dr. D. Geiger (University of Ulm) for assistance in conducting the TEM investigations, and E. Schmid (University of Ulm) for ultramicrotomy of our samples. We thank Dr. U. Burkhardt (MPI CPfS) for the measurement of EDX and WDX spectra, Dr. G. Auffermann (MPI CPfS) for ICP-OES measurements, and Dr. T. Leichtweiss (University of Gießen) for XPS spectra. We are indebted to Dipl.-Ing. U. C. Rodewald (University of Münster) for collecting the single-crystal X-ray data. This work was supported by the Deutsche Forschungsgemeinschaft.

Supporting information for this article is available on the WWW under http://dx.doi.org/10.1002/anie.201402244.

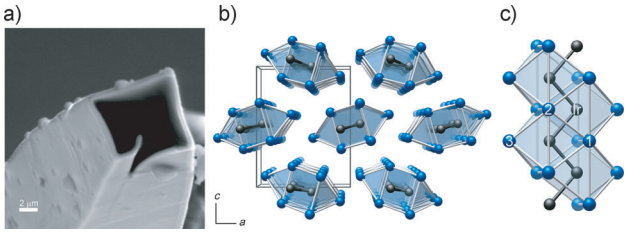

Figure 2. Single-crystal morphology and structure of Bi_3Ir. a) Hollow intergrowth structure of Bi_3Ir crystals obtained from a bismuth flux. b) Crystal structure of Bi_3Ir consisting of a pseudo-hexagonal packing of $^1_\infty[IrBi_{6/3}Bi_{1/1}]$ rods. c) Side view of a rod showing iridium atoms that are coordinated by seven bismuth atoms in the shape of a capped trigonal prism. The prisms share their rectangular faces and thereby form zigzag chains of iridium atoms.

compound is far from trivial to obtain. The standard metallurgical approach—basically crystallization from a homogenous high-temperature melt—is strongly hampered by the drastic differences in the fundamental physical properties of the two elements: bismuth evaporates 800 K below the melting point of iridium (2410 °C)![5] Furthermore, the solubility of iridium in liquid bismuth is only 3 % at 1100 °C. Early investigations of the Bi–Ir system by melt reactions and subsequent annealing resulted in the binary phases Bi_2Ir and Bi_3Ir.[6,7] The structure types $CoSb_2$ and Bi_3Ni were assigned on the basis of Debye–Scherrer photographs. However, later studies on transition-metal arsenopyrites could not reproduce Bi_2Ir or any other binary Bi–Ir phase, neither in annealing experiments nor by chemical transport reactions.[8]

One option for the synthesis of binary bismuth–iridium compounds could be the application of high pressure to suppress the evaporation of bismuth, in analogy to the synthesis of Bi_3Co, which is not accessible under ambient pressure.[9] So far, this approach has not yielded Bi_3Ir. Alternatively, iridium can be provided in more reactive forms: We obtained Bi_3Ir single crystals in low yield from the intermetallic precursor $Sm_3Ir_3Sb_7$, which was dissolved in molten bismuth at 1100 °C, while phase-pure samples of Bi_3Ir nanoparticles became available when we reduced the metal salts in a microwave-assisted polyol process at 230 °C, a method that had already been applied to synthesize phase-pure Bi_3Ni,[10] Bi_2Ir,[11] and BiRh nanoparticles.[12] While the shape of the nanoparticles is unremarkable, the larger crystals obtained from the flux showed the unusual intergrowth morphology of hollow square tubes (Figure 2a).

X-ray diffraction on single crystals obtained by the intermetallic precursor method confirmed the predicted orthorhombic (*Pnma*) Bi_3Ni-type structure (Figure 2b) with lattice parameters $a = 8.970(2)$ Å, $b = 4.190(6)$ Å, and $c = 11.511(5)$ Å ($V = 432.6(1)$ Å^3) at 20 °C. For the nanoparticles of Bi_3Ir slightly different lattice parameters of $a = 8.900(2)$ Å, $b = 4.170(1)$ Å, and $c = 11.602(3)$ Å ($V = 430.6(2)$ Å^3) were determined (Figure S1 in the Supporting Information). The iridium atoms are coordinated by seven bismuth atoms in the shape of a capped trigonal prism. The Bi–Ir distances range from 2.76 to 2.92 Å, comparable to the sum of the covalent radii[5] of 2.78 Å. By sharing their rectangular faces the trigonal prisms form $^1_\infty[IrBi_{6/3}Bi_{1/1}]$ rods (Figure 2c). Thereby, the iridium atoms arrange in zigzag chains with short Ir–Ir distances of 2.80 Å. A substantially reduced electron density on the iridium position was best explained by mixed occupancy (EDX/WDX analyses, see Table S1 and Figure S4 in the Supporting Information) according to the formula $Bi_3(Ir_{0.77}Cu_{0.17}Ni_{0.06})$ for this crystal. No structural deformation or superstructure could be detected, neither by X-ray or electron diffraction (ED) nor by transmission electron microscopy (TEM). High-resolution TEM imaging exhibits equidistant zigzag chains of transition-metal atoms (Figure S5 in the Supporting Information). Angle-dependent structure refinements also ruled out possible artifacts created by the tremendous absorption of X-rays (the linear absorption coefficient $\mu(Mo_{K\alpha})$ of Bi_3Ir is 153 mm^{-1}; the lead[13] of the primary beam stop has "only" 139 mm^{-1}). Apparently the copper and nickel traces in the elemental bismuth that has been used for synthesis accumulate in the flux-grown crystals. Crystals containing a lower amount of 3d metals have also been identified.

The absorption of oxygen is observed only for Bi_3Ir nanoparticles. The Bi_3Ir crystals obtained by the intermetallic precursor method do not show the effect. In fact, the nanoparticles grown by the microwave-assisted polyol process are much smaller (maximum of the size distribution at 60 nm) and have an amorphous shell (Figure 3a) that contains besides organic molecules also bismuth and iridium cations, as can be deduced from TEM contrast and X-ray photoelectron spectroscopy. This shell seems to be essential for the activation of molecular oxygen, since the reactivity is dramatically reduced when the shell is removed. The latter is possible by plasma cleaning of the TEM samples and also

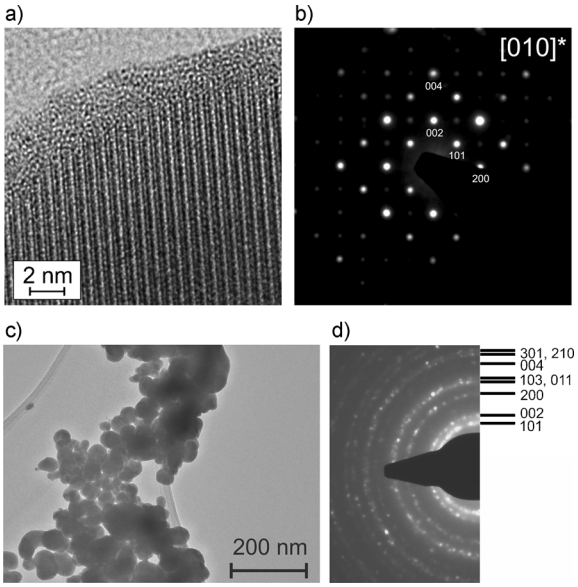

Figure 3. Electron microscopy and diffraction of Bi_3IrO_x. a) Bi_3IrO_x ($x \approx 1$) particle at high resolution revealing an amorphous shell surrounding the crystalline core. b) A selected electron diffraction pattern of a particle after plasma cleaning. The presence of forbidden reflections is due to double-diffraction phenomena. c,d) Bright-field imaging and an indexed ring diffraction pattern of Bi_3IrO_x powder. From both the spot and ring ED patterns, the lattice parameters of $a = 9.44$ Å, $b = 3.8$ Å, $c = 12.7$ Å for $x \approx 1$ can be deduced.

improves the quality of the ED patterns of the Bi_3IrO_x crystals (Figure 3b and Figure S6 in the Supporting Information). Nonetheless, the oxygen uptake is a volume effect as has been shown by PXRD, ED, and quantitative monitoring of the oxygen pressure in a closed cell during oxygen uptake (see below). The reciprocal space sectioning of Bi_3IrO_x nanoparticles confirms that their crystal structure is very similar to that of intermetallic Bi_3Ir except for minor changes in unit cell parameters ($a = 9.44$ Å, $b = 3.8$ Å, $c = 12.7$ Å for $x \approx 1$ from ED).

Alternatively, Bi_3IrO_x can be synthesized within minutes by treating Bi_3Ir nanoparticles with aqueous H_2O_2 solution (30%). We also observed that Bi_3Ir nanoparticles remove physically dissolved molecular oxygen from ethanol at room temperature.

Because the combination of small nanoparticles and extreme X-ray absorption effects are not conducive to conventional Rietveld refinement, structure models for Bi_3IrO_x were developed by quantum chemical means and the calculated diffraction diagrams were compared to the observed patterns. Based on the expansion of the inter-rod distances in the Bi_3Ir structure three possible positions for oxide ions were identified. With two of these positions occupied, three possible models can be constructed. DFT-based geometry optimization yielded stable structures in all cases. The one with lowest total energy is displayed in Figure 4. Its calculated diffraction pattern nicely matches the measured powder diffractogram of the oxidized sample (Figure S2 in the Supporting Information).

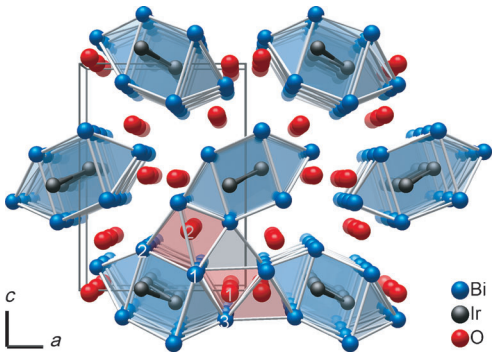

Figure 4. Crystal structure of Bi_3IrO_2 projected along the intermetallic rods (*b* axis). The increase in the distances between the rods generates space for oxide ion diffusion and storage. Besides tetrahedral and octahedral sites that are occupied by oxide ions (red), additional tetrahedral voids (gray) are available for mass transport and further oxygen uptake.

In Bi_3IrO_2, one type of oxide ions has four bismuth neighbors, the other type six. Bi–O bond lengths range for the tetrahedral coordination from 2.23 to 2.45 Å (average 2.34 Å), for the octahedral case from 2.26 to 2.99 Å (average 2.66 Å). The bond-valence concept[14] provides a rough estimate of the strength of the oxygen fixation compared to that of known bismuth oxides. In α-Bi_2O_3,[15] the bond-valence sums of the three crystallographically independent oxide ions, that is, the sum of all O–Bi bonding interactions, are 1.93, 1.98, and 2.05. In the case of γ-Bi_2O_3[16] and δ-Bi_2O_3,[16] which are fast oxide ion conductors at temperatures above 650 °C,[17,18] these valence sums are only 0.69, 1.18, and 1.30 (γ-Bi_2O_3), or 1.69 (δ-Bi_2O_3). Bond-valence sums of 2.07 and 1.64 indicate that the integration of at least one of the oxide ions in Bi_3IrO_2 is also comparatively weak. Moreover, the diffusion paths between the intermetallic rods are straight and there is an excess of closely spaced voids with low hopping barriers between them. The combination of these advantageous factors nicely explains the observed ultrahigh mobility of oxide ions even at room temperature.

For an intermetallic compound, Bi_3Ir is unusually electron-rich. The highest occupied states close to the Fermi level are involved in bonding between bismuth atoms of neighboring rods, as can be deduced from the band dispersion in the directions orthogonal to the rods (Figure 5a: Γ-X and Γ-Z). The partial ELI-D for the states close to the Fermi level shows that they originate mainly from the lone pairs of bismuth atoms and have minor impact on the bonding between metal atoms within a single rod (Figure 5e). Upon oxidation, these states are depopulated and the inter-rod bonding is replaced by electrostatic interactions between positively charged bismuth atoms and oxide ions. Still, the material remains metallic (Figure 5b). A combined *k*-space and real-space

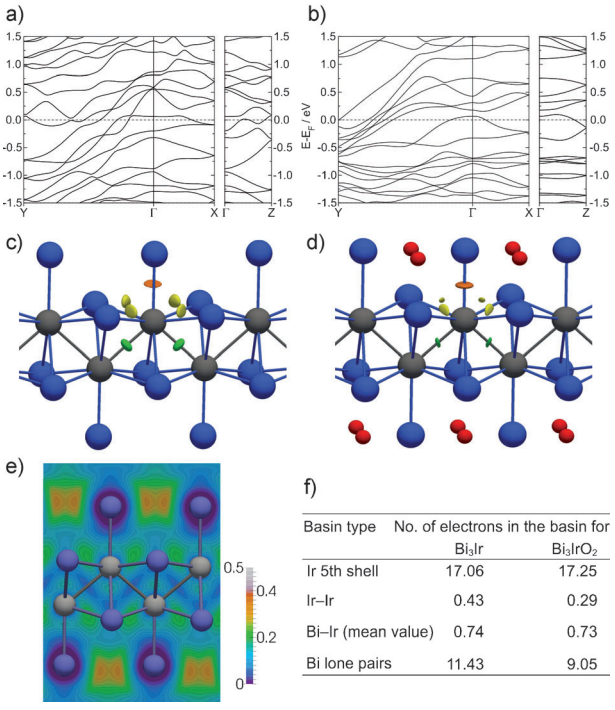

Basin type	No. of electrons in the basin for	
	Bi_3Ir	Bi_3IrO_2
Ir 5th shell	17.06	17.25
Ir–Ir	0.43	0.29
Bi–Ir (mean value)	0.74	0.73
Bi lone pairs	11.43	9.05

Figure 5. Electronic band structure and real-space bonding indicators for Bi_3Ir and Bi_3IrO_2. a,b) Band structure plots along the paths shown in Figure S8 in the Supporting Information for Bi_3Ir and the Bi_3IrO_2, respectively. c,d) Localization domains of the ELI-D indicator, which mark bonding between two Ir atoms (green) and between Ir and Bi atoms (capping Bi3: orange; Bi1 and Bi2: yellow). The isosurface values for the yellow and orange domains are near 1.0 and for the green domains 0.96 in Bi_3IrO_2 (d) and 0.97 in Bi_3Ir (c). e) Partial ELI-D (pELI-D) diagram for the states in the interval −1.6 eV to 0 eV, which corresponds to approximately 4 electrons per formula unit. f) The total number of electrons in selected ELI-D basins, showing that oxidation affects primarily the Bi atoms.

bonding analysis (Figure 5c,d) revealed that the sum of Bi–Ir bonds, which are governing the bonding inside the rods, is indifferent to an oxygen content up to at least $x = 2$. While the Ir–Ir bonding is somewhat weakened, the number of electrons on the iridium atom and thereby its oxidation state remain unchanged. As the bismuth atoms remain strongly bonded to iridium, they are not available for the formation of Bi_2O_3, which would be expected as the trivial product of the oxidation. Nonetheless, the bismuth atoms are oxidized. With respect to the crystallographically independent atoms, the charge distribution in Bi_3Ir can be approximated as $Bi1^{+0.5}Bi2^{+0.5}Bi3^{\pm 0}Ir^{-1}$, while in Bi_3IrO_2 it is close $Bi1^{+1.5}Bi2^{+1.5}Bi3^{+2}Ir^{-1}(O^{-2})_2$. The capping bismuth atom, Bi3, is most affected by oxidation; however, its bonding to the iridium atom is not weakened, according to the total number of electrons found in bonding basins (Figure 5f). A similar situation has been found in the stable subhalides of Bi_3Ni.[19,20]

The X-ray diffraction experiment shows the instantaneous formation of the second phase with a larger unit cell in the early stages of the oxygen uptake. Based on LeBail refinement, the lattice parameters change by $\Delta a = +5.0\,\%$, $\Delta b = -5.8\,\%$, $\Delta c = +9.5\,\%$ and the volume by $\Delta V = +8.3\,\%$. The elongation of a and c axes refers to an increase in the distance between the prism rods and opens the space for oxygen intercalation. The absolute volume change is approximately 39 Å^3. The radius of 1.42 Å for a highly coordinated oxide ion tabulated by Shannon and Prewitt[21,22] corresponds to an isotropic volume of 11.5 Å^3. Taking typical packing densities ($\leq 72\,\%$) into account, the expected maximum of the oxygen uptake (x) should be about two oxide ions per formula unit. This prediction is corroborated by the effective volume of 18 Å^3 for an oxide ion, which was given by Biltz.[23] The difference between the chemical analyses of freshly synthesized Bi_3Ir nanoparticles and an oxidized sample (air, 20 d, 20 °C) likewise suggests an oxygen uptake of $x = (2.0 \pm 0.2)$ atoms per formula unit. Yet, the analyses are assumed to be biased by the organic shell.

In contrast to the single-stage expansion of the structure, monitoring of the pressure in an oxygen-filled chamber shows that after a rapid initial uptake of oxygen by the intermetallic nanoparticles, the process continues at a moderate, almost constant rate (Figure 6a). This suggests an initial structural expansion step that is followed by subsequent diffusion-controlled filling of the generated channel system. The negligible incubation time is in accordance with a topotactical reaction mechanism and suggests very low activation energies, including the activation of the double bonds in the oxygen molecules. If one applies the ideal gas law, compositions of $Bi_3IrO_{1.0}$ after 30 h and $Bi_3IrO_{1.8}$ after 96 h at 25 °C can be deduced. An increase in temperature by 5 °C results in Bi_3IrO_2 after only four days. Within the same period the composition Bi_3IrO_3 can be attained if the reaction temperature is 45 °C. Exposure to pure oxygen atmosphere at 60 °C ultimately results in irreversible oxidation to Bi_2O_3 and precipitation of elemental iridium. The presence of humidity during the oxidation seems to lower the activation energy of the oxidation process, which is reflected in a faster initial uptake of oxygen (Figure S7 in the Supporting Information).

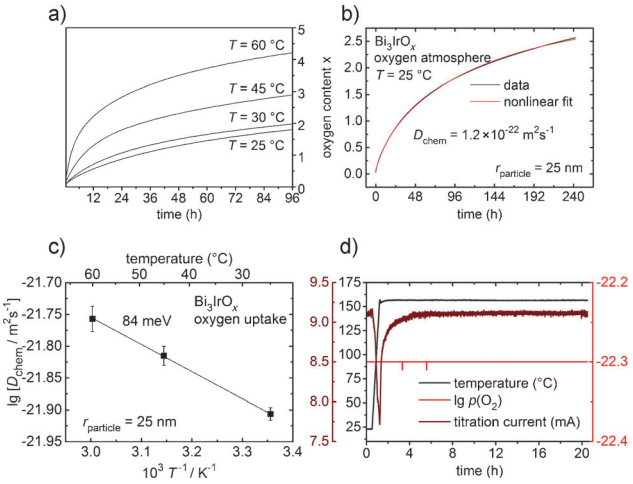

Figure 6. Oxygen uptake, reversibility, and kinetics of oxygen diffusion. a) Oxygen uptake at different temperatures in an oxygen-filled chamber. b) Profile of the absorption of dry oxygen in a pressure cell at 25 °C and the derived oxygen diffusion coefficient. c) Temperature dependence of the chemical diffusion coefficient and activation energy for oxide transport in Bi_3IrO_x. d) Coulometric titration of a sample that was stored in air at room temperature for four days. The reduction process in argon/hydrogen atmosphere at 150 °C already started during the heating process at 30 °C and was finished after six hours. The total oxygen content per formula unit of the starting material is calculated to be $x = 0.31$.

The profiles of the absorption of dry oxygen in the pressure cell at 25, 45, and 60 °C were fit with a model for reactions controlled by one-dimensional diffusion of a gaseous species into a spherical solid including the exchange coefficient of the surface (Figure 6b). The fits show that the intercalation is predominantly controlled by diffusion. The diffusion coefficient of 1.2×10^{-22} m^{2}s^{-1} appears unimpressive compared to that of YSZ (10^{-19} m^{2}s^{-1} at 150 °C),[24] yet the value was determined at 25 °C! Hence the diffusion of oxygen ions inside the solid is unprecedentedly fast in this temperature regime. The linear fit of the temperature dependence of the diffusion coefficients reveals an unmatched low activation energy of only 84 meV (Figure 6c). Typical values for the anion transport in oxides range from 0.8 to 1.0 eV.

Bi_3IrO_x ($x \leq 2$) can be fully reduced to the intermetallic compound Bi_3Ir by treatment with hydrogen. A coulometric titration of oxygen in an OXYLYT device[25] in argon/hydrogen atmosphere (Figure 6d) demonstrates that the reduction process starts already at about 30 °C. After 6 h at 150 °C the reduction is complete. Alternatively, solution-based reduction can be performed at room temperature by using hydrazine (80 vol% in aqueous solution) or Superhydride (lithium triethylborohydride; 1 M in THF). Upon repeated oxidation and complete reduction the material becomes progressively amorphous and the activity for oxygen uptake decreases drastically. It has to be tested how the degree of oxygen loading and unloading influences the cycling capability.

In conclusion, Bi_3Ir proved to be an astonishing material, especially in nanocrystalline form. Its ability to activate molecular oxygen at room temperature, either from the gas

phase or physically dissolved in solvents, by reversible redox intercalation could be exploited for sensors, electrodes of solid oxide fuel cells, and oxidation catalysts. Bi_3IrO_x is the first metallic oxide ion conductor and also the first that operates at room temperature, showing unusually low activation energy for oxygen ion transport.

Received: February 10, 2014
Published online: May 27, 2014

Keywords: intermetallic phases · ion conductors · metastable compounds · subvalent compounds · topochemistry

[1] M. S. Whittingham, A. J. Jacobson, *Intercalation Chemistry*, Academic Press, New York, **1982**.
[2] T. Enoki, M. Suzuki, M. Endo, *Graphite Intercalation Compounds and Applications*, Oxford University Press, New York, **2003**.
[3] W. Müller-Warmuth, R. Schöllhorn, *Progress in Intercalation Research*, 2nd ed., Springer, Berlin, **2012**.
[4] S. M. Auerbach, K. A. Corrado, P. K. Dutta, *Handbook of Layered Materials*, CRC, New York, **2004**.
[5] J. Emsley, *The Elements*, Oxford University Press, New York, **1998**.
[6] N. N. Zhuravlev, E. M. Smirnova, *Sov. Phys. Crystallogr.* **1966**, *10*, 694 – 697.
[7] T. B. Massalski, H. Okamoto, P. R. Subramanian, in *Binary Alloy Phase Diagrams*, *2nd ed.* (version 1.0), ASM International, **1996**.
[8] A. Kjekshus, *Acta Chem. Scand.* **1971**, *25*, 411 – 422.
[9] U. Schwarz, S. Tencé, O. Janson, C. Koz, C. Krellner, U. Burkhardt, H. Rosner, F. Steglich, Y. Grin, *Angew. Chem.* **2013**, *125*, 10038 – 10042; *Angew. Chem. Int. Ed.* **2013**, *52*, 9853 – 9857.
[10] T. Herrmannsdörfer, R. Skrotzki, J. Wosnitza, D. Köhler, R. Boldt, M. Ruck, *Phys. Rev. B* **2011**, *83*, 140501.
[11] R. Boldt, A. Grigas, M. Heise, T. Herrmannsdörfer, A. Isaeva, S. Kaskel, D. Köhler, M. Ruck, R. Skrotzki, J. Wosnitza, *Z. Anorg. Allg. Chem.* **2012**, *638*, 2035 – 2043.
[12] D. Köhler, M. Heise, A. I. Baranov, Y. Luo, D. Geiger, M. Ruck, M. Armbrüster, *Chem. Mater.* **2012**, *24*, 1639 – 1644.
[13] A. R. Stokes, A. J. C. Wilson, *Proc. Phys. Soc. London* **1941**, *53*, 658 – 662.
[14] N. E. Brese, M. O'Keeffe, *Acta Crystallogr. Sect. B* **1991**, *47*, 192 – 197.
[15] S. A. Ivanov, R. Tellgren, H. Rundlöf, V. G. Orlov, *Powder Diffr.* **2001**, *16*, 227 – 230.
[16] H. A. Harwig, *Z. Anorg. Allg. Chem.* **1978**, *444*, 151 – 166.
[17] T. Takahashi, H. Iwahara, *Mater. Res. Bull.* **1978**, *13*, 1447 – 1453.
[18] H. A. Harwig, A. G. Gerards, *J. Solid State Chem.* **1978**, *26*, 265 – 274.
[19] M. Ruck, *Z. Anorg. Allg. Chem.* **1997**, *623*, 243 – 249.
[20] M. Ruck, *Z. Anorg. Allg. Chem.* **1999**, *625*, 453 – 462.
[21] R. D. Shannon, C. T. Prewitt, *Acta Crystallogr. Sect. B* **1969**, *25*, 925 – 946.
[22] R. D. Shannon, *Acta Crystallogr. Sect. A* **1976**, *32*, 751 – 767.
[23] W. Biltz, *Raumchemie der festen Stoffe*, Leopold Voss, Leipzig, **1934**.
[24] R. Röwer, G. Knöner, K. Reimann, H. E. Schaefer, U. Södervall, *Phys. Status Solidi B* **2003**, *239*, R1 – R3.
[25] K. Teske, H. Ullmann, N. Trofimenko, *J. Therm. Anal.* **1997**, *49*, 1211 – 1220.

